ADVANCED FUNCTIONAL MATERIALS
www.afm-journal.de

Disinfector-Assisted Low Temperature Reduced Graphene Oxide-Protein Surgical Dressing for the Postoperative Photothermal Treatment of Melanoma

Yuanhao Wu, Junyao Yang, Alexander van Teijlingen, Alice Berardo, Ilaria Corridori, Jingyu Feng, Jing Xu, Maria-Magdalena Titirici, Jose Carlos Rodriguez-Cabello, Nicola M Pugno, Jiaming Sun, Wen Wang, Tell Tuttle, and Alvaro Mata**

Materials that combine the functionalities of both of proteins and graphene are of great interest for the engineering of biosensing, drug delivery, and regenerative devices. Graphene oxide (GO) offers an opportunity to design GO-protein interactions but the need for harsh reduction processes to enable GO photoexcitation remains a limitation. A disinfector-assisted low temperature method to reduce GO-protein materials and fabricate surgical dressings with tuneable photothermal efficiency and bioactive properties for the postoperative treatment of melanoma is reported. The approach harnesses the capacity of 70% ethanol to penetrate the protein shell of microorganisms to infiltrate GO-protein complexes and reduce GO at low temperature (85 °C) while maintaining the material structure and bioactivity. Both experiments and coarse-grained simulations are used to describe the reduction process and assess the material properties. In vitro and in vivo validation revealed the capacity of the dressings to prevent tumor recurrence and promote healing after tumor resection.

1. Introduction

Surgical resection is normally used to treat cutaneous melanoma[1,2] but can lead to postoperative recurrence.[3] In this case, a large, expanded resection of normal tissue surrounding the original tumor is required to attempt to remove any residual melanoma cells,[4] which in turn leads to delayed healing. As a result, therapeutic methods such as chemotherapy and immunotherapy are being used in combination with surgical procedures to treat cutaneous melanoma. However, such targeted therapies are reported to be easy for tumor cells to develop resistance to and exhibit limited effectiveness[5] and immunotherapies are only used for advanced (stage 4) melanoma, which cannot be

Y. Wu, A. Mata
School of Pharmacy
University of Nottingham
Nottingham NG7 2RD, UK
E-mail: a.mata@nottingham.ac.uk

Y. Wu, A. Mata
Department of Chemical and Environmental Engineering
University of Nottingham
Nottingham NG7 2RD, UK

Y. Wu, A. Mata
Biodiscovery Institute
University of Nottingham
Nottingham NG7 2RD, UK

The ORCID identification number(s) for the author(s) of this article can be found under https://doi.org/10.1002/adfm.202205802.

[+]Present address: Department of Civil, Environmental and Architectural Engineering, University of Padova, via Marzolo 9, Padova 35131, Italy
[++]Present address: BIOtech Center for Biomedical Technologies, Department of Industrial Engineering, University of Trento, via delle Regole 101, Trento 38123, Italy

DOI: 10.1002/adfm.202205802

Y. Wu, W. Wang, A. Mata
Institute of Bioengineering
Queen Mary University of London
London E1 4NS, UK

Y. Wu, N. M. Pugno, W. Wang, A. Mata
School of Engineering and Materials Science
Queen Mary University of London
London E1 4NS, UK

Y. Wu, J. Sun
Department of Plastic Surgery
Union Hospital
Tongji Medical College
Huazhong University of Science and Technology
Wuhan 430022, China

J. Yang
Department of Clinical Laboratory
Xinhua Hospital, School of Medicine
Shanghai Jiao Tong University
Shanghai 200092, China

A. van Teijlingen, T. Tuttle
Department of Chemistry
University of Strathclyde
Glasgow G1 1XL, UK
E-mail: tell.tuttle@strath.ac.uk

removed using surgery.[6] In contrast, photothermal therapy (PTT) is a promising method for local and accurate cancer treatment, which relies on local heating of the tumor through injecting photothermal agents (PTAs) that transform the energy of light into heat.[7] However, injecting PTAs has been applied in small animal models with limited volume of melanoma tumor,[8] which can be challenging in human cases that tend to exhibit large tumors with limited blood flow to transport PTAs.[9] With this in mind, the combination of surgery and PTT offers combined benefits to remove large tumors and inhibit recurrences. Surgical dressings are essential to cover the post-operative trauma to protect the defective tissue, but traditional surgical dressings such as pads and gauzes tend to be inert and have no function in stimulating anti-tumor activity, nor promoting healing. Consequently, an ideal surgical dressing for the treatment of melanoma would precisely offer PTT to eliminate residual tumor cells, reduce the expanded area of resection, and inhibit tumor recurrence, while simultaneously causing angiogenesis and regenerating tissues.

Graphene (G) and reduced graphene oxide (rGO) are being explored as PTAs given their capacity for high absorbance in the near-infrared (NIR) region and low cost.[10] However, dispersed G and rGO exhibit dose-dependent toxicity to cells,[11,12] which can be significantly decreased by combining them with biomolecules such as DNA[13] or albumin[14] to aggregate and cover dispersed G/rGO sheets. Nevertheless, these combinations can be difficult to achieve due to difficulties in dispersing of G/rGO in solvents resulting from a lack of oxygen-containing groups in G/rGO sheets.[15] Alternatively, graphene oxide (GO) can be combined with peptides, proteins, or biopolymers to generate uniform materials exhibiting rich oxygen-containing groups for stable suspension and intermolecular interactions.[16] These GO-biomolecule complexes exhibit low cytotoxicity[17] and biologically relevant mechanical properties such as bending, beating, and twisting to recreate the physical function,[18,19] however, with low PTT efficiency to transfer NIR light to heat. As a result, rGO is more widely used in the medical field as an anti-tumor PTA than GO due to its high NIR response,[20,21] low risk of side effects,[22] and higher biocompatibility than G both in vitro[23] and in vivo.[24]

A. Berardo,[+] I. Corridori,[++] N. M. Pugno
Laboratory of Bioinspired, Bionic, Nano
Meta Materials & Mechanics
Department of Civil
Environmental and Mechanical Engineering
University of Trento
via Mesiano 77, Trento 38123, Italy
J. Feng, M.-M. Titirici
Department of Chemical Engineering
Imperial College London
London SW7 2AZ, UK
J. Xu
Department of Pediatric Orthopedics
Xinhua Hospital
School of Medicine
Shanghai Jiao Tong University
Shanghai 200092, China
J. C. Rodriguez-Cabello
BIOFORGE Group
University of Valladolid
CIBER-BBN, Valladolid 47011, Spain

The reduction of GO requires an anhydrous ethanol environment in a sealed reactor with high temperatures of at least 180 °C,[25] which would denature GO-biomolecule complexes and eliminate any benefits that could potentially be generated by the biomolecules. Addressing this need, Stankovich et al[26] and Gao et al[27] demonstrated that polymers and amino acids can help decrease the temperature necessary for reduction of GO-containing systems to as low as 80 °C. Consequently, it may be possible to develop a GO reduction method capable of removing oxygen-containing groups from GO at low temperatures within GO-biomolecule materials without damaging the biomolecules and preserving their properties.

We have recently reported on a co-assembling GO-disordered protein system capable of generating robust membranes at liquid–liquid interfaces.[28] The membranes are assembled by cooperative interactions between GO flakes and an elastin-like recombinamer (ELR) named ELK1 with structure MESLLP-$(VPGIG\ VPGIG\ VPGKG\ VPGIG\ VPGIG)_{24}$. The resulting co-assembled membrane consists of multi-layered supramolecular ensembles exhibiting core-shell structures with GO cores and ELR shells. ELRs are known to promote dermal repairing and wound healing.[29] Ethanol has been used as an effective reagent for the reduction of GO.[30] Furthermore, it is known that 70% ethanol can penetrate bacteria and the protein shell of viruses to serve as an antiseptic and general clinical disinfector.[31,32] Consequently, in this study, we investigated the potential of 70% ethanol to penetrate the protein (ELR) shell and into the GO core to reduce GO at low temperatures and generate functional rGO-ELR membranes while simultaneously sterilizing the material. Therefore, we report on a disinfector-assisted low temperature method to reduce GO-protein materials and engineer surgical dressings for PTT of melanoma. The dressings exhibit both high PTT efficiency and the capacity to promote tissue regeneration. Based on both experiments and coarse-grained simulations, we describe the underlying mechanism of GO-ELR reduction and PTT effectiveness, and demonstrate the potential of the dressings for the postoperative treatment of melanoma both in vitro and in a murine model.

2. Results and Discussion

2.1. Rationale of the Study

The study is based on our ELK1-GO material because of its multi-layered hierarchical structure and biocompatibility.[18,28] Emulating the way ethanol is able to infiltrate the protein shell of microorganisms, we used ethanol to penetrate the ELK1 shell (**Figure 1**a) of the ELK1-GO complex (Figure 1b). 70% ethanol was used because lower ethanol concentrations exhibit less penetration while higher concentrations lead to coagulation of proteins in bacteria[33] and viruses.[34] Penetration of the ELK1 shell enables and enhances infiltration within the GO layers that make up the GO core (Figure 1c) to facilitate reduction of GO while maintaining relatively low temperatures (Figure 1d). We designed this process to be performed at 85 °C, which is the highest reaction temperature we can use that is just below the boiling temperature of 70% ethanol. Consequently, we are able

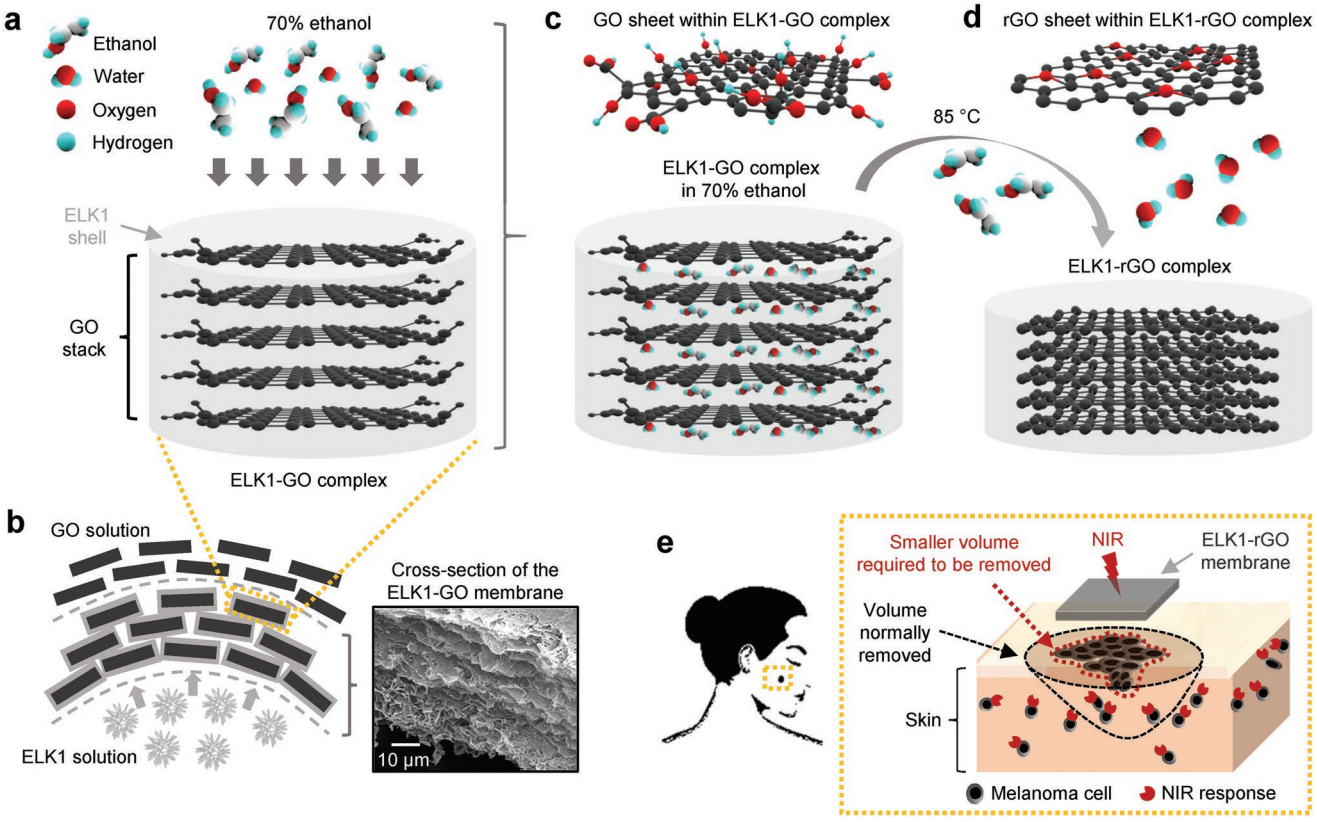

Figure 1. Rationale of the ELK1-GO membrane reduction process and application. Illustration depicting a). exposure of 70% ethanol to an ELK1-GO complex comprising stacks of GO. b). ELK1-GO complexes form multi-layered ELK1-GO membranes, which are co-assembled at the interface of a GO solution and an ELK1 solution.[28] c). Ethanol molecules penetrate the ELK1 protein shell and bind the oxygen-containing groups present on the GO sheets. d). Upon heating up to 85 °C, the GO sheets lose oxygen-containing groups resulting in GO reduction (rGO) and, consequently, a decrease in the thickness of the ELK1-rGO complex. e). Illustration depicting the use of the resulting ELK1-rGO membranes as surgical dressings for the postoperative NIR treatment of melanoma. The photo-thermal therapy (PTT) efficiency of the surgical dressings would enable much smaller surgical resections (area within red dashed line) compared to normal procedures requiring large resections (area within black dashed line). The NIR treatment would also enable elimination of residual melanoma cells.

to enhance the efficiency of the GO reduction process while maintaining both a relatively low temperature and the ELK1-GO material structure. The resulting ELK1-GO membrane could serve as a robust and antiseptic surgical dressing for the effective photothermal therapy (PTT) of melanoma while exhibiting its capacity to stimulate the growth of endothelial cells[35] and promote wound healing (Figure 1e).

2.2. Material Characterization and Mechanism of GO Reduction

2.2.1. Reduction of GO within the ELK1-GO Membranes

We first aimed to confirm that 70% ethanol would offer optimum penetration and reduction of the ELK1-GO complex. To do this, ELK1-GO membranes were immersed in different ethanol concentrations (0%, 50%, 70%, 100%) at 85 °C for 48 h. Fourier transform infrared spectroscopy (FT-IR) spectra revealed that the heating treatment led to a reduction in typical peaks of oxygen-containing groups [−OH (3340 cm^{-1}), C=O (1730 and 1630 cm^{-1}), and C−O (1226 and 1044 cm^{-1})] in all samples except 0% ethanol (**Figure 2**a,b). As expected, 70% ethanol led to the largest decrease, which indicates the highest removal of oxygen-containing groups from ELK1-GO materials and the highest potential for GO reduction. Raman spectroscopy confirmed this finding with typical double peaks of D band and G band located at 1343 and 1590 cm^{-1}, respectively, and the highest ID/IG ratio for the 70% ethanol group (Figure 2d). Having established the optimum ethanol concentration, we then investigated the effect of time and kinetics of GO reduction. ELK1-GO membranes were heated to 85 °C in 70% ethanol for 0, 8, 24, or 48 h (referred to as ELK1-rGO-reduction time) (Figure 2e). Using both FT-IR and Raman spectroscopy, we conducted a step-by-step GO reduction process (Figure 2c–e) with gradient decreases of peaks in oxygen-containing groups and increase of ID/IG ratios. Finally, to confirm that the ELK1 was not removed during the heating process, we used X-ray photoelectron spectroscopy (XPS) to identify nitrogen-containing groups, which are only present in ELK1 molecules (Figure 2f). The peaks of N−C=O and C−N are present within the ELK1-GO complex both before and after 70% ethanol treatment. Furthermore, the atomic concentration (Atomic%) of N element increased from 11.39% (before heating) to 15.06% (after heating for 48 h) (Figure 2f, red insert) due to a similar loss

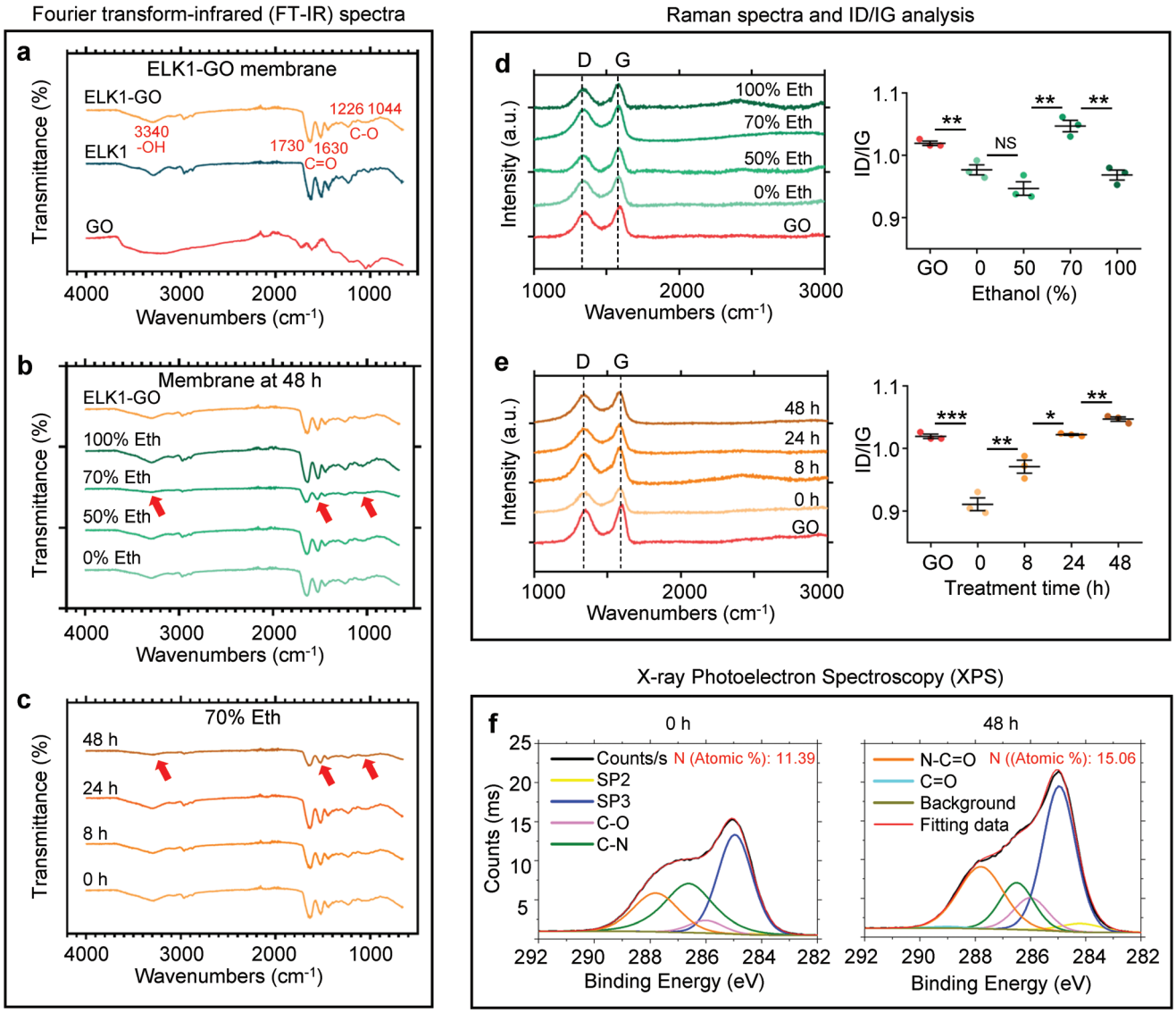

Figure 2. Assessment of the GO reduction process within the ELK1-GO membrane. a). FT-IR spectra of ELK1-GO membranes showing the oxygen containing groups -OH (3340 cm^{-1}), C=O (1730 and 1630 cm^{-1}), and C—O (1226 and 1044 cm^{-1}) in ELK1-GO (orange graph) from combination of ELK1 (blue graph) and GO (red graph). b). FT-IR spectra of ELK1-rGO membranes exposed to different concentrations of ethanol identifying the 70% ethanol concentration as optimum for enhanced removal, and c). step-by-step removal of oxygen-containing groups in ELK1-rGO with increasing reduction time. d). Raman spectra of ELK1-rGO membranes exposed to different concentrations of ethanol revealing the highest ID/IG (most effective) for 70% ethanol and e). step-by-step reduction of GO with increasing reduction time. f). XPS of ELK1-rGO membrane exposed to 70% ethanol for 0 and 48 h demonstrating the existence of ELK1 in ELK1-rGO with nitrogen-containing groups (green graph C—N and orange graph N—C=O) after 48 h reduction. Atomic concentration of N element increasing from 11.39% (before heating) to 15.06% (after heating for 48 h) (Red insert). Error bars present ± s.d. *$p < 0.05$.

of Atomic% of O element (Table S8, Supporting Information). These results demonstrate that our heating method effectively removed oxygen-containing groups from the GO within the ELK1-GO complex, reducing GO while maintaining the ELK1 components.

2.2.2. Wide-Angle X-Ray Scattering and Coarse-Grained Simulation Confirm the Reduction of GO within ELK1-GO Membranes

To confirm GO reduction and provide mechanistic insight into the process, we conducted wide-angle x-ray scattering (WAXS) and coarse-grained simulations to identify the interlayer distance between the GO sheets within the GO core. We hypothesized that removal of oxygen-containing groups from GO would decrease the distance between rGO sheets and result in nanostructural changes. Therefore, WAXS analysis provided a precise measurement of the interlayer distance of rGO sheets[36] within the GO core for ELK1-rGO membranes treated for 20 h in different ethanol concentrations (0%, 50%, 70%, and 100%) and for different reduction times (0, 8, 24, 48, or 72 h) in 70% ethanol. The results revealed that the 70% ethanol treatment led to the smallest GO interlayer distance (4.03 Å) and that increasing treatment times resulted in higher GO interlayer

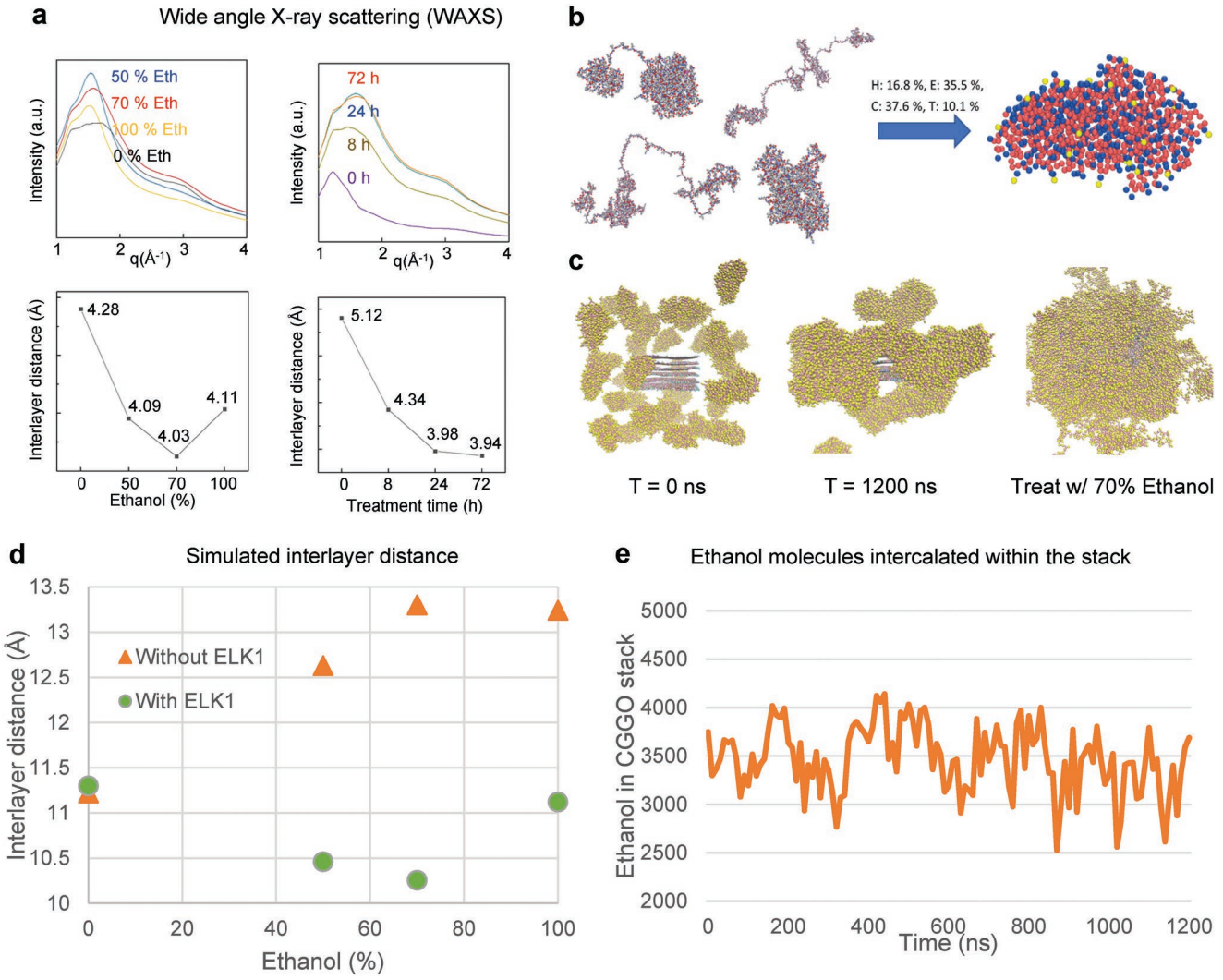

Figure 3. Assessment of GO reduction within the ELK1-rGO complex by WAXS and coarse-grained simulations. a). WAXS graphs of ELK1-rGO complex reduced by different concentrations of ethanol revealing 70% ethanol having the shortest interlayer distance (4.03 Å) between rGO sheets (left panel), and the interlayer distance decreasing with increasing reduction time (right panel). b). Four conformers of the ELK1 protein being suggested by the Robetta server, equilibration of the coarse-grained structure finding the disordered protein to collapse to the same structure from each starting point with the Lys groups (yellow) orientated towards the solvent. c). Snapshots of the CGMD simulation showing the dispersed ELK1 proteins aggregating on the surface of the GO stack, particularly around the edges of COO- groups, once equilibrated with 70% ethanol the tertiary and quaternary structure of the protein being severely disrupted leading to a greater coverage of the GO stack. d). The change in solvent/co-solvent system towards increasing alcohol increasing interlayer distance between GO sheets (orange triangles), and the GO stack the interlayer distance decreasing when the ELK1 protein being complexed with, indicating a greater probability for reactivity around 70% ethanol (green dots). e). The simulations of the flow of ethanol molecules into and out of the stack demonstrating ability of ethanol molecules to penetrate the ELK1-GO complex structure.

distance reductions (peak shift corresponding to carbon 002 plane) from 5.12 Å at 0 h to 3.94 Å at 72 h (**Figure 3**a). Interestingly, for 0% ethanol (Figure 3a, top left, black curve), no reduction was observed due to absence of the reductant, which resulted in no effect peak in GO interlayer distance as recorded in the q range from 1 to 2 ($Å^{-1}$) using WAXS. The presence of a peak in this WAXS analysis is due to a uniform interlayer distance of GO sheets within the ELK1-GO material. It has been reported that water is responsible for micro-explosions on GO sheets at relative low temperatures (≈80 °C) after overnight treatment.[37] The heating process that was used to treat "0%Eth" destroys this interlayer structure and consequently does not exhibit a peak in WAXS. This result demonstrates that ethanol was essential to reduce GO.

To confirm these findings, we conducted coarse-grained simulations of the ELK1-GO system, initially in water at room temperature to investigate the co-assembly of the randomly arranged ELK1 proteins with a stack of 6 GO sheets (Figure 3b,c; and Section S1, Supporting Information) for details of the model construction and simulation parameters. The assembly of the ELK1-GO system is largely driven by electrostatic attraction and confirm that the bulk of the protein aggregation occurs at the edges of the sheets where carboxylate groups are present as opposed to the faces of the stack (Figure 3c).

Once the ELK1-GO systems are assembled, the boxes are resolvated with 0, 50, 70, and 100% ethanol with the temperature coupled to 85 °C and equilibrated for a further 4.8 μs each. We find that the coverage of ELK1 increases with the increase in temperature, ethanol and concentration and find that the structure with the lowest z distances is observed at 70% ethanol (Figure 3d, green dots). However, in the absence of the ELK1 protein the opposite is true, i.e., the GO sheets are exfoliated[38] as the concentration of ethanol is increased (Figure 3d, orange triangles). The compression of the GO sheets at 70% ethanol in the presence of ELK1 increases reactivity between ethanol and the GO leading to greater reduction. The decrease in interlayer spacing is also consistent with that observed experimentally. Though the simulated distances are significantly larger, which is partially a result of the bead size in the CG model (Section S1, Supporting Information). However, it is also consistent with the need for ethanol to migrate between the sheets in order for reduction to be possible. Indeed, we observe that even at 70% ethanol (the minimum interlayer spacing modelled) the amount of ethanol between the GO sheets fluctuates significantly (≈3500 ± 350 ethanol beads between the GO sheets, Figure 3e) during the simulation – indicating that ethanol is still able to flow throughout and reduce the GO sheets. The increased reduction is consistent with the decreased spacing observed experimentally for the dried rGO samples (Figure 3a).

2.2.3. Structure and Mechanical Properties of ELK1-rGO Membranes

The decrease in interlayer distance within the GO core as a result of the GO reduction led to thinner membranes with smoother surfaces and cross-sections (**Figure 4**a). These microstructural changes were expected owing to restored C—C or C—O—C covalent bonds within GO sheets as well as conformational changes in GO sheets and ELK1 molecules. These structural alterations in the ELK1-rGO membranes led to changes in mechanical properties, which were investigated via nanotensile testing following established protocols (Figure 4b).[28,39] ELK1-rGO membranes exhibited higher Young's moduli (E) (Figure 4c) and strengths (σ) (Figure 4d), but no differences were observed in strain at break compared to unreduced membranes (Section S2, Supporting Information). The highest Young's moduli were observed on ELK1-rGO-48 h (≈1100 kPa) and 72 h (≈1284 kPa), which were at least 143% higher than ELK1-GO-0 h.[28] Interestingly, membranes kept in 70% ethanol solution but without heating exhibited a Young's modulus

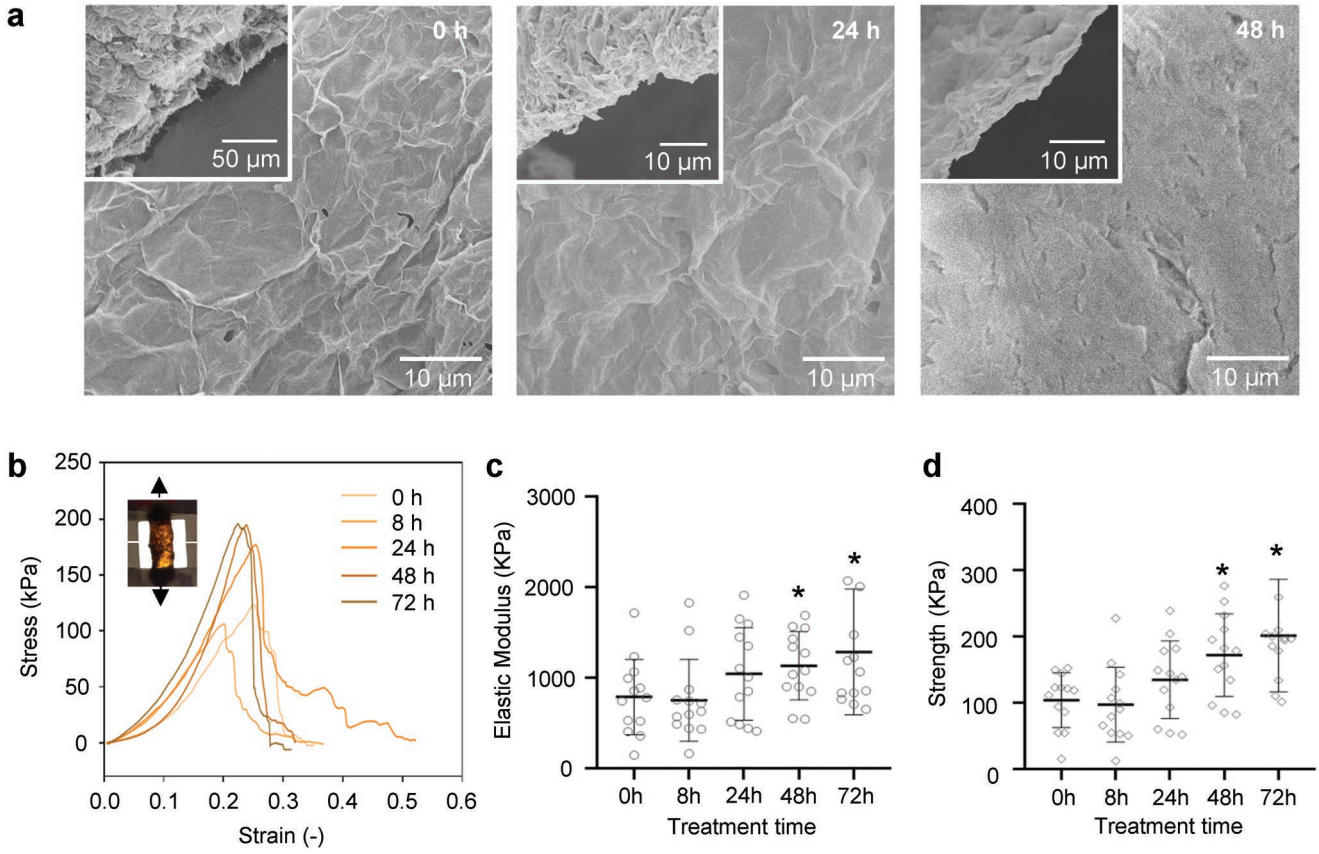

Figure 4. Improvement of structural integrity and mechanical properties. a). SEM images depicting the surface structure of ELK1-rGO membranes and differences in their respective thickness (inserts), which decrease with increasing reduction time in 70% ethanol. This membrane thickness reduction results from the removal of oxygen-containing groups, which decrease interlayer distances between GO sheets. b). Graphs from nanotensile tests of ELK1-rGO membranes revealing an improvement of elastic modulus c) and strength d) with longer reduction times (48 and 72 h) in 70% ethanol. Thirteen samples were tested for each reduction time. Error bars present ± s.d. *$0.01 < p < 0.05$, **$p < 0.01$.

and strength increase of 88% and 125%, respectively, compared to membranes in pure water (Section S2, Supporting Information). We speculate that this increase resulted from dehydration of the membranes in 70% ethanol. These results demonstrate that the 70% ethanol GO reduction treatment increased membrane stiffness but did not affect the strain at break, resulting in more robust and elastic membranes. These properties of the ELK-rGO membranes would facilitate their use as surgical dressings because of the possibility to conform to the specific anatomical region and tightly cover the wound.

2.2.4. Assessment of PTT Efficiency

We then assessed the PTT efficiency of ELK1-rGO membranes, which is defined as the relation between NIR treatment time and environmental temperature increase. ELK1-rGO membranes (ELK1-rGO-8, 24, 48, and 72 h) were placed at the bottom of 24-well plates and immersed in 1 mL PBS. An 808 nm NIR light source (1 W cm^{-2}) was applied from the bottom of the plate and temperature changes in the PBS were measured. As expected, temperature increases occurred faster in membranes with higher levels of GO reduction (**Figure 5**a). Given the specific application of the current study, we focused the experiments on generating temperatures of 50 °C, which is the temperature required to guarantee killing of tumor cells.[40] The results revealed that only 1 min was required to reach 50 °C in ELK1-rGO-48 h and ELK1-rGO-72 h membranes compared to untreated membranes which took 5 min. We have compared the ELK1-rGO membrane with other PTA-based composite materials including an oligomeric proanthocyanidins hydrogel[41] and a 2D Ge-based material,[42] which have been developed for similar applications in skin cancer treatment. The temperature conduction efficiency of our ELK1-rGO material was higher than that of an oligomeric proanthocyanidins hydrogel and a 2D Ge-based material. Under NIR irradiation at the same power density of 1.0 W cm^{-2} to increase 20 °C of PBS environmental temperature, 1 cm^2 oligomeric proanthocyanidins hydrogels needed 400 s and 1 cm^2 2D Ge-based materials needed 300 s, while 0.35 cm^2 ELK1-rGO-48 h needed 30 s. The smaller size ELK1-rGO-48 h enabled a similar temperature increase but in a shorter period of time. The possibility to apply shorter NIR treatments could lead to improved curative effects because of less pain and damage generated by the heating process. These results demonstrate that 48 h was an optimum 70% ethanol reduction time, with similar PTT efficiency to ELK1-rGO-72 h but requiring less reduction time.

2.3. Biological Validation Toward a Surgical Dressing

2.3.1. Human Umbilical Vein Endothelial Cells and B16 Melanoma Cell Proliferation

CCK-8 assays were conducted using human umbilical vein endothelial cells (hUVECs) and B16 melanoma cells to assess the potential applicability of the membranes for the treatment of melanoma in vitro. CCK-8 assays were first conducted to measure the proliferation of B16 melanoma cells and hUVECs on ELK1-rGO membranes. Different ELK1-rGO membranes (ELK1-rGO-8, 24, 48, and 72 h) were positioned at the bottom of 96-well plates and inoculated with 2500 cells/membrane. After 24 h of cell culture, the general trend was that both hUVEC and B16 melanoma cell proliferation decreased with increasing GO reduction time. However, the lowest cell proliferation was observed on ELK1-rGO-0 h for hUVECs and on ELK1-rGO-48 h for B16 melanoma cells (Figure 5b), which may result from differences in the material's surface smoothness and oxygen-containing groups.[43] The groups containing less oxygen hinder migration but groups exhibiting smoother surfaces promoted adhesion. The reduction process decreased the oxygen-containing groups of the ELK1-rGO composite while increasing the surface smoothness of the material as evidenced by FT-IR and scanning electron microscopy (SEM) (Figure 2a–c and Figure 4a). hUVEC and B16 melanoma cells responded with different preferences of migration and adhesion to surface conditions under different reduction times. These results demonstrate that ELK1-rGO-48 h membranes inhibited B16 melanoma cell proliferation while supporting the growth of hUVECs.

2.3.2. hUVEC and B16 Melanoma Cell Adhesion and Live/Dead Assay

To confirm the effects on cell migration and adhesion, we then cultured hUVECs or B16 melanoma cells directly on top of 0.35 cm^2 ELK1-rGO membranes positioned at the bottom of 48-well plates. This setup allowed us to assess cell adhesion and migration at the edge of the membranes. ELK1-rGO-48 h membranes were tested while ELK1-rGO-8 h membranes were used as control given our results demonstrating that they support the growth of both cell types (Figure 5c, illustration). Dead/live assays were conducted at 24 h of culture and revealed extensive growth of hUVECs with very few dead cells on the top of both ELK1-rGO-8 h and ELK1-rGO-48 h membranes. The cells seemed to adhere tightly on both membranes and migrated continuously from the bottom of the well to the membrane. B16 melanoma cells exhibited a similar growth behaviour as hUVECs on ELK1-rGO-8 h membranes. However, B16 melanoma cells were unlikely to adhere to the edge of ELK1-rGO-48 h membrane, which formed a clear gap with very few cells between the well surface and the ELK1-rGO-48 h membrane (Figure 5c). These results confirm that ELK1-rGO-48 h membranes supported hUVECs growing but inhibited B16 melanoma cells adhering and migrating. Furthermore, in combination with the mechanical properties (Figure 4b) and PTT efficiency results (Figure 5a), these results reveal the potential of our process and resulting ELK1-rGO-48 h membranes to be used for PTT.

2.4. In Vitro Experiments to Assess Potential for PTT of Melanoma

2.4.1. Optimization of NIR Treatment Time to Inhibit Recurrence of B16 Melanoma Cells

In vitro experiments were conducted to assess the efficiency of ELK1-rGO-48 h to potentially inhibit recurrence of melanoma cells via PTT and identify a suitable NIR treatment frequency.

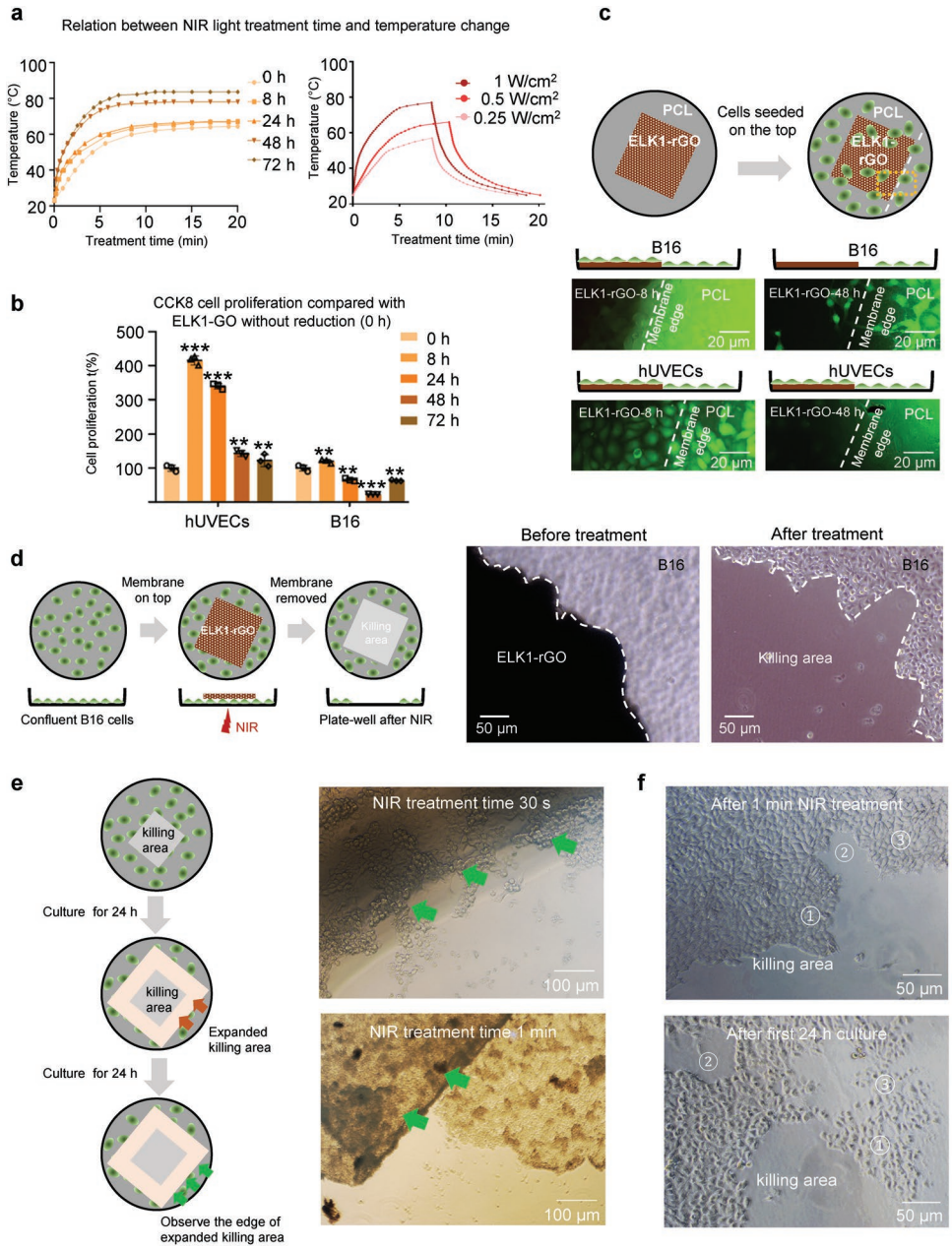

Figure 5. Photothermal treatment (PTT) efficiency and assessment of in vitro performance. a). Graphs (left) of relationship between NIR treatment time and temperature of ELK1-rGO membranes reduced for different times by the 70% ethanol method demonstrating PTT efficiency of ELK1-rGO membranes increasing with increasing reduction time. Graphs (right) of ELK1-rGO-48 h membranes under different powers (0.25, 0.5, 1 W cm^{-2}) of laser irradiation followed by free convection cooling. b). CCK8 assay identifying the proliferation of hUVECs and B16 melanoma cells after culturing for 48 h on ELK1-rGO membranes reduced by 70% ethanol for different times. c). hUVECs or B16 melanoma cells cultured for 24 h on top of ELK1-rGO membranes positioned at the bottom of 48-well plates. Dead (red)/live (green) assays revealing growth of hUVECs or B16 melanoma cells on ELK1-rGO-8 h and ELK1-rGO-48 h membranes. d). Generated killing area (grey square area) of hUVECs or B16 melanoma cells underneath an ELK1-rGO-48 h membrane. Optical images depicting the killing area of B16 melanoma cells surrounding the contour of the membrane. e). Expanded killing area (pink) generated by irradiation surrounding original killing area (grey) after 24 h culture, observing edges of expanded killing area of cell migrating (green arrows) back to killing area after another 24 h culture. Optical images of edges of expanded killing area of B16 melanoma cells after either 30 s or 1 min NIR treatment revealing B16 cells migrating back into the killing area with 30 s NIR treatment time. These cells were observed to be detaching from the bottom of the well with 1 min treatment time. f). Optical images of edges of original killing area of hUVECs migrating back (labels ①②③ referring to the same areas of hUVECs before and after the 24 h culture period) into killing area demonstrating that the 1 min NIR treatment does not generate an expanded killing area. Error bars present ± s.d. $*p < 0.05$.

B16 melanoma cells were cultured to >95% confluency on 48-well plates. Membranes (≈0.35 cm^2 surface area) were then positioned directly on top of the cells and 1 mL PBS was added into the well. A 1 cm^2 808 nm NIR light source (1 Wcm^{-2}) was used to irradiate from the bottom of the wells toward the membranes (Figure 5d, illustration) for either 30 s or 1 min. These

treatment times were used to reach between 50 and 60 °C to kill the tumor. After NIR treatment, a clear "killing area" was observed only directly below the ELK1-rGO-48 h membranes (Figure 5d), demonstrating the capacity of the membranes to deliver PTT. In contrast, unirradiated membranes did not affect the cells directly underneath, confirming the killing effectiveness of the NIR treatment and not any kind of physical touch from the membrane on the cells. Furthermore, the thermal radiation emerging from the membrane was able to kill more B16 melanoma cells around the original killing area within 24 h after irradiation and generate an expanded killing area of about 200% of the area directly underneath the membrane (Figure 5d, illustration).

To further characterize the effectiveness of the thermal radiation treatment, we continued the cultures for another 24 h. We found that B16 melanoma cells were able to migrate back toward the "killing area" defined by the original treatment with the 30 s NIR treatment but not with those exposed 1 min NIR. In fact, cells surrounding the "killing area" in these 1 min treated samples were observed to detach from the well (Figure 5e). Hence, we believe that the thermal radiation treatment is effective and could be tailored to optimize a potential PTT of melanoma.

2.4.2. Effect of NIR Treatment on hUVECs

An ideal treatment for melanoma would enable both effective killing of tumor cells as well as stimulation of healthy cells to facilitate regeneration of the tissue. Based on the capacity to tailor the thermal treatment and the propensity of hUVECs to grow on the ELK-GO material (Figure 5b,c), we then investigated NIR treatment effects on hUVECs following a similar experimental setup as that used with B16 melanoma cells. After a 1 min NIR treatment, which was able to completely kill B16 melanoma cells, hUVECs also died directly underneath the membrane but, unlike B16 melanoma cells, were able to rapidly migrate and repopulate the "killing area" within 24 h (Figure 5f). These results demonstrate that the NIR treatment did not generate continuously negative effects on hUVECs and indicate the possibility to use our membranes for PTT to kill melanoma cells but facilitating regrowth of vascular tissue.

2.5. In Vivo Experiments to Assess Potential for PTT of Melanoma

2.5.1. Effectiveness of PTT by Hematoxylin and Eosin Staining

To confirm the potential of our membrane for PTT of melanoma, we then conducted in vivo experiments using melanoma subcutaneous tumor C57BL mice models.[44] Biocompatibility was assessed in vivo and confirmed via blood routine tests, urinalysis, liver, and kidney function tests, and histological hematoxylin and eosin (H-E) staining of mice organs after implantation with the ELK1-rGO-48 h for 15 days (Section S3, Supporting Information). For the formal in vivo experiments, the mice were anesthetized, and the melanoma tumors were surgically resected just around the edge of the melanoma tumor without expanded resection after 10 days of planting of tumor. Four groups with different NIR treatment times were tested including a blank control-15 s (no material but NIR treated for 15 s), GO-15 s (GO alone and NIR treated for 15 s), ELK1-rGO-15 s (ELK1-rGO-48 h and NIR treated for 15 s), and ELK1-rGO-30 s (ELK1-rGO-48 h and treated for 30 s). These treatment times were used to avoid minor skin burns that can develop for longer exposures.[45] The materials were placed directly on top of the postoperative wounds, sealed with tissue glue, and treated by NIR once every 48 h to inhibit the recurrence of melanoma cells as previously described (Figure 5d,e). At day 7, the mice were sacrificed and the materials along with the surrounding tissues were removed and fixed with wax for histological analysis. H-E staining clearly revealed the profile of the materials (inside yellow dash lines) and surrounding tissues (**Figure 6**a). Residual melanoma cells (black arrows) were observed only in blank control and demonstrated that PTT materials effectively kill the melanoma cells. However, obvious vacuolar necroses of epidermal cells (red arrows) were found only in the GO-15 s group indicating a significant side-effect resulting from inflammation. It has been reported that GO particles in water suspension are cytotoxic at high concentrations (>500 μg mL^{-1}) and can stimulate the activation of inflammatory responses.[46] However, our co-assembling method decreased the toxicity of GO due to aggregation of GO sheets and the localization of the ELK1 on the sharp edges of GO sheets[28] but still kept the PTT property. As expected, ELK1-rGO-15 s and ELK1-rGO-30 s groups displayed a well-organized tissue near the wound and clear interfaces between the materials and surrounding tissues. No inflammatory response or residual melanoma cells were observed in ELK1-rGO-48 h groups. These results demonstrate that our membrane effectively killed the melanoma in vivo without any observable side-effect through PTT.

2.5.2. Optimization of NIR Treatment Time In Vivo by Immunohistochemistry Staining

To confirm the elimination of melanoma cells and optimize the NIR treatment time to enable a potential angiogenic response post-treatment with our membranes, Ki67 and CD31 were labeled (Figure 6b) to demonstrate the presence of B16 melanoma cells and hUVECs, respectively. Both ELK1-rGO-15 s and ELK1-rGO-30 s groups did not show any residual B16 melanoma cells, but only ELK1-rGO-15 s displayed clear endothelial cells growing within the tissue, particularly surrounding the edge of the membrane, suggesting that angiogenesis (yellow arrows) is taking place in the treated animals. This result confirmed that 15 s NIR treatment time was able to kill melanoma cells but at the same time enable angiogenesis, which suggest the possibility to both inhibit recurrence of melanoma and promote healing of the wound.

2.5.3. Anti-Melanoma and Wound Healing Functions In Vivo by Wound Healing Experiments

Using the optimum PTT parameters (ELK1-rGO-48 h, 15 s NIR treatment time, once every 48 h), anti-melanoma and wound

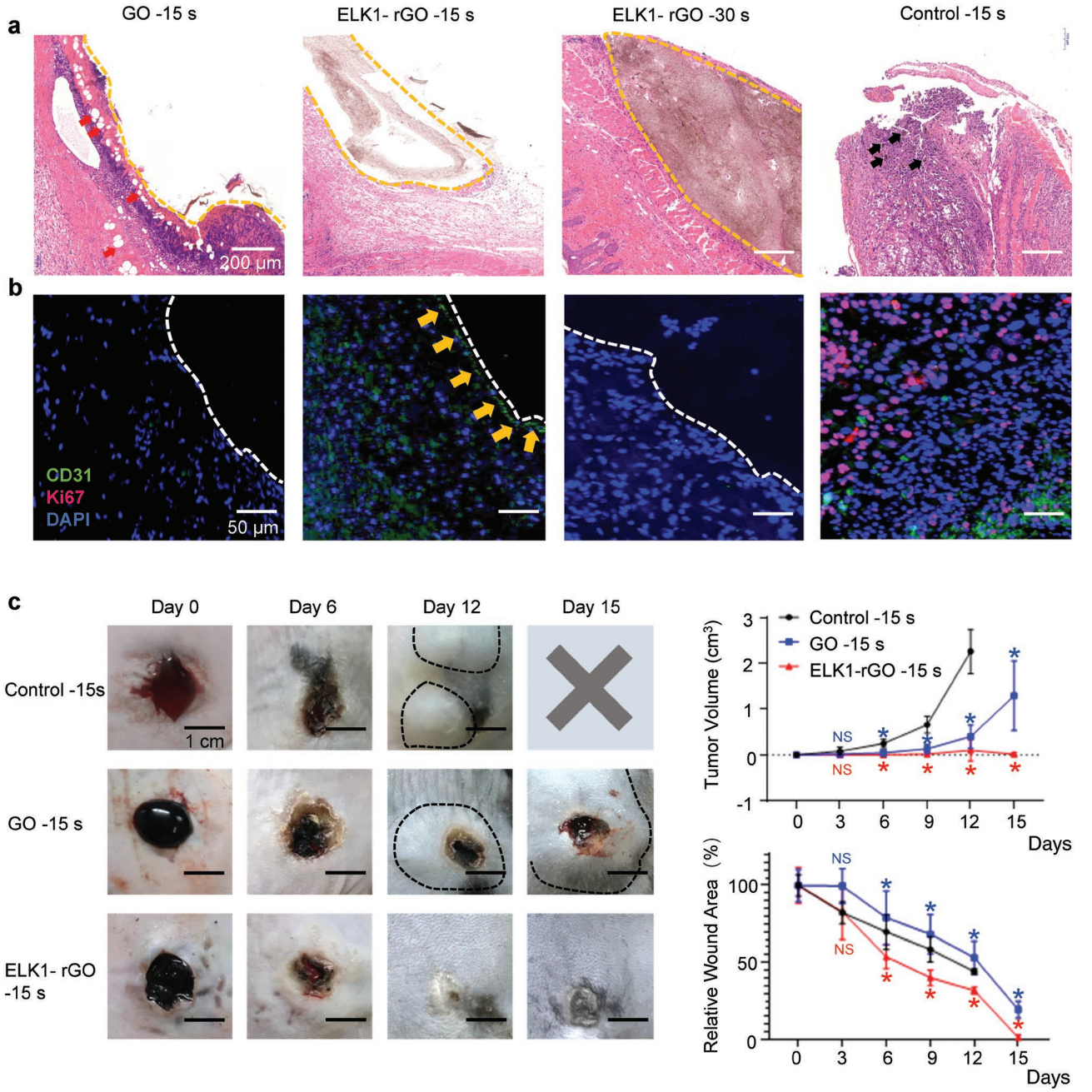

Figure 6. In vivo assessment of inhibition of melanoma recurrence and promotion of wound healing. a). Histological sections of materials and surrounding tissues from four tested groups including Control-15 s (no material but NIR treated for 15 s), GO-15 s (GO alone and NIR treated for 15 s), ELK1-rGO-15 s (ELK1-rGO-48 h and NIR treated for 15 s), and ELK1-rGO-30 s (ELK1-rGO-48 h and treated for 30 s). H-E staining illustrating the profiles of the materials (inside yellow dash lines) and surrounding tissues. ELK1-rGO-15 s and ELK1-rGO-30 s groups with well-organized tissue near the wound and clear interfaces between the materials and surrounding tissues. Vacuolar necrosis of epidermal cells (red arrows) in the GO-15 s group indicating serious inflammatory responses, and residual melanoma cells (black arrows) in blank group indicating PTT materials is required to eliminate residual melanoma cells. b). CD31 (endothelial cell marker, green), Ki67 (tumor cell marker, pink), and DAPI (blue) were labeled to demonstrate the elimination of melanoma cells and optimize the NIR treatment time (15 s) enabling a potential angiogenic (yellow arrows) response post-treatment. c). Photographs of wounds after 15 s NIR treatments at Day 0, 6, 12, and 15 indicating an inhibition of melanoma recurrence (inside black dash lines) and promotion of wound healing in ELK1-rGO-48 h group. Graphs of quantitative measurement of tumor volume and relative wound area at Day 0, 3, 6, 9, 12, and 15 after operation. Data is obtained from three independent experiments, six mice per group. Error bars present ± s.d. $*p < 0.05$.

healing functions were investigated through a wound healing experiment (Figure 6c, images). Three groups of materials (Blank control-15 s, GO-15 s, ELK1-rGO-15 s) were applied as surgical dressings following similar methods as described above. Tissue glue was used to fix the materials for all groups and the wound healing process was recorded using a camera.

The results revealed that the wound of ELK1-rGO-15 s group completely healed at Day 15 post-treatment. In contrast, the mice treated with both blank control and GO groups exhibited an obvious recurrent melanoma by Day 6 (inside black dash lines). For the blank control group, mice were sacrificed before the end of the experiments at Day 15 because the sizes of recurrent tumors were larger than those approved by our ethical committee. The relative wound area and tumor size change between different groups at Day 15 (Figure 6c, graph) demonstrated the efficiency of the ELK1-rGO-48 h membrane to be used as a PTT postoperative surgical dressing to both inhibit the recurrency of melanoma and promote wound healing. This capability would offer significant patient advantages in applications that require both clinical surgery and PTT.

3. Conclusion

GO-protein composites offer great advantages for biomedical devices but the need for harsh GO reduction processes has limited their use. Here, we have introduced a simple low temperature GO reduction method and demonstrated its capacity to develop rGO-protein materials with photothermal conductivity and bioactive properties. Through both experimental and simulation evidence, we have described the molecular mechanism of the reduction process and established methodologies to developed functional rGO-protein materials. Using these methodologies, we have developed photothermal postoperative dressings and validated their capacity to both prevent cancer recurrence and enhance healing of the surgical site in a murine model.

4. Experimental Section

Chemicals: GO (product number 777 676) was obtained from Sigma–Aldrich. ELR [ELK1: MESLLP-(VPGIG VPGIG VPGKG VPGIG VPGIG)$_{24}$] molecule was provided by TP Nanobiotechnology (Valladolid, Spain), synthesized and purified by Escherichia coli recombinant expression system. Ethanol (product number 459 836) was purchased from Sigma–Aldrich.

Sample Preparation of ELK1-GO and Ethanol-Assisted Reduction Treatment: Aqueous suspension of GO (0.1 wt%, 100 µl) was added to a well of 96-well TCP and aqueous solution of the ELK1 (2 wt%, 18 µl) was slowly injected into the suspension of GO. The tip of the pipette was allowed to contact the bottom of the well before releasing the ELK1 solution vertically at a constant speed. All samples were prepared in MilliQ water. The ELK1-GO membranes were opened from vertical tubular samples and immersed in different ethanol concentrations (0%, 50%, 70%, and 100%), Then the samples and solvent were sealed in a Teflon reactor and heated up to 85 °C for different reduction times (0, 8, 24, 48, or 72 h).

Fourier Transform Infrared Spectroscopy: Fourier transform infrared spectroscopy (FT-IR) analysis was conducted on FT-IR spectrometer (Cary 630 FT-IR Spectrometer, Agilent Technologies, Santa Clara, USA). ELK1–rGO membranes were prepared as previous description and frozen dried. Membranes were properly secured over the IR window before scanning. The program was set to take the cm^{-1} average of 160 scans at a resolution of 2 after subtracting the background and cm^{-1} spectra were obtained at wavenumber 4000–600 with respect to the absorbance for all samples.

Raman Spectroscopy: Raman spectroscopy was performed on a 514 mm wavelength using a Senterra II spectrometer (Bruker, Billerica, Massachusetts, US). When analyzing, freeze-dried samples were placed on a glass slide, and the Raman spectra were collected between 500 and 3000 cm^{-1}. The peak positions and the intensities were determined by the combination of Gaussian–Lorentzian line shapes in OriginPro 2020.

X-Ray Photoelectron Spectroscopy: X-ray photoelectron spectroscopy (XPS) analysis was performed using a Nexsa XPS system with a monochromated Al-Kα X-ray source (h_{υ} = 1486.6 eV, Thermo Scientific, Waltham, Massachusetts, US). Before the XPS analysis, the samples were freeze-dried and placed on the samples stage with copper tape. The obtained XPS data were analyzed and fitted using Avantage software.

Scanning Electron Microscopy: The microstructures of ELRs–GO and ELK1–GO membranes ELK1–rGO membranes were dehydrated directly using increasing concentrations of ethanol (20, 50, 70, 90, 96, and 100%). All samples were subjected to critical point drying (K850, Quorum Technologies, UK) prior imaging. The scanning electron microscopy (SEM) micrographs were captured on Inspect F50 (FEI Comp, the Netherlands) after sputter-coating with gold (10 nm thick).

Wide-Angle X-Ray Scattering: Wide Angle X-ray Scattering (WAXS) samples preparation and analysis. Freeze-dried samples were loaded on to samples holder, and the samples test was performed in beamline I22 (SM28002, Diamond Light Source, UK), Diamond Light Source, UK. Beam energy was 12.4 keV with a wavelength of 1 Å. Data was collected as a stack of 100 × 0.1 s frames and averaged.

Cell Culture: Mouse tumor cell lines B16-F10 were obtained from the Chinese Academy of Sciences Cell Bank of Type Culture Collection and cultured in Dulbecco's Modified Eagle's Medium (DMEM; Gibco, Life Technologies) with 10% (v/v) fetal bovine serum (FBS, Gibco), 0.01 mg mL^{-1} insulin and 100 units mL^{-1} penicillin/streptomycin (HyClone). Human umbilical vein endothelial cells (HUVECs) were obtained from ScienCell Research Laboratories and cultured in basal endothelial cell medium (EBM2) supplemented with the EGM-2-MV bullet kit (CC-3156; Lonza). All of the cells cultured in a humidified incubator at 37 °C and 5% CO2/95% air (v/v).

In Vitro Viability and Cytotoxicity: The biocompatibility and cytotoxicity of the ELK1-GO against B16-F10 and HUVECs were evaluated by the CCK-8 test in vitro. Typically, different ELK1-rGO members were positioned at the bottom of 96-well plates, then B16-F10 or HUVECs cells were seeded in 96-well plates with a density of 2.5 × 10^3 cells per well. After incubating for 24 h, the cells were washed with PBS and 100 µL of CCK-8 solution (0.5 mg mL^{-1}) was added to each well for another 4 h culture according to the manufacturer's guidelines (C0041, Beyotime). After that, cell viability was assessed by the absorbance at 450 nm on the microplate reader (Biotek Synergy2, Winooski, VT, USA). HUVECs or B16-F10 melanoma cells directly on top of 0.35 cm^2 ELK1-rGO membranes positioned at the bottom of 48-well plates. After 24 h, Dead/live assays were performed to evaluate the number of damaged cell, according to the manufacturer's guidelines (Calcein/PI Cell Viability/Cytotoxicity Assay Kit, Beyotime). The cells were photographed using an Olympus CKX53 Imaging System (Olympus Corporation) with an excitation wavelength of 495 nm.

In Vivo Experiments of Tumor Growing and Wound Healing: 4–6-week-old male C57BL/6J mice were purchased from Shanghai Laboratory Animal Center of China. All animal breeding, housing and experimentation was conducted according to the guidelines of the Institutional Committee of Shanghai Jiao Tong University School of Medicine for Animal Research (Approval No. XHEC-F-2020-026). Specifically, animals were housed in a controlled environment with a 12 h light/dark cycle, with free access to water and food and at temperatures of 21–23 °C and humidity of 40–60%.

In vivo tests were carried out 3 times using 6 mice in each group. Online random number generators (e.g., https://www.graphpad.com/quickcalcs/randomize1/) was used to allocate mice to groups ensures that each group has an equal probability of receiving a particular treatment and provides balanced numbers in each treatment group. The mice were monitored continuously until being sacrificed. Melanoma-developing mice were monitored and euthanized at an endpoint defined by adverse clinical symptoms, such as multiple skin tumors Ø > 5 mm, weight loss (△m > 15%) or a hunched back.

Low passage B16-F10 cells were resuspended in a 1:1 mixture of PBS and Matrigel (Corning #356 231) at 1×10^6 cells mL^{-1}. 100 µl of cell stock was injected subcutaneously on the shaved right flank of C57BL/6J mice. After10 days' growing, the tumor volume increased to an average size of 80 mm^3. Tumors were excised along the edges, PBS, GO, or ELK1-GO was administered on the postoperative trauma and covered with tissue gel (3 M Vetbond Tissue Adhesive 1469c). The surgical area with material was treated with or without NIR irradiation for 15 s or 30 s once every 48 h. When the diameter of tumor exceeded 1.5 cm, the mice would be sacrificed. The samples of materials with surrounding tissues were excised and fixed in 4% formaldehyde solution for H-E staining or immunofluorescence staining.

The tumor size was measured using a digital caliper, and the tumor volume was calculated using the formula: volume = $0.5 \times \text{width}^2 \times$ length. For the wound area measurement, photographs of the wound was taken using a Canon 10-megapixel camera (Canon, Tokyo, Japan). Care was taken to ensure that the true margins of each wound were completely visible. Images were calibrated to scale and were analyzed using Image J software (National Institutes of Health, Bethesda, Md) to trace wound margins and calculate surface area. Each wound area was then expressed as a percentage of its original area on day 1 (just prior to treatment).

Immunofluorescence Staining: The immunofluorescence was performed by staining with a rabbit polyclonal antibody against human/mouse CD31 (1:200; ab28364, Abcam), Ki67(1:200; ab15580, Abcam), and a Goat Anti-Rabbit IgG H&L (Alexa Fluor 488) (1:200; ab150077, Abcam) as previously described. Then cells were mounted with ProLong Gold antifade Reagent with DAPI (Life Technologies). Images were captured using Leica SP5 Laser scanning confocal microscope.

Hematoxylin and Eosin Staining: H-E staining was conducted according to routine protocols. Briefly, after deparaffinization and rehydration, tissue sections were stained with haematoxylin solution (ZSGB-BIO, China) for 5 min followed by 5 dips in 1% acid ethanol (1% HCl in 75% ethanol) and then rinsed in double distilled water. Then the sections were stained with eosin solution (ZSGB-BIO, China) for 3 min and followed by dehydration with graded alcohol and clearing in xylene. Images were captured using Leica SP5 Laser scanning confocal microscope.

Statistical Analysis: The data expressed as the mean ± standard error of the means were analyzed using GraphPad Prism 9 with a *t* test for pairwise comparisons or analysis of variance, followed by multiple comparison tests for comparisons involving more than two groups, and significance was depicted by asterisks, $*P<.05$; A value of $P<0.05$ was considered to be significant.

Supporting Information

Supporting Information is available from the Wiley Online Library or from the author.

Acknowledgements

Y.W. and J.Y. contributed equally to this work.The work was supported by the ERC Starting Grant (STROFUNSCAFF), the Medical Research Council (UK Regenerative Medicine Platform Acellular/Smart Materials 3D Architecture, MR/R015651/1), and the AO Foundation AOCMF-17-19M. The WAXS experiment at the Diamond Light Source was allocated beamtime under experiment number SM28002 and collected on I22. JCRC is grateful for the funding from the Spanish Government (PID2019-110709RB-100, RED2018-102417-T), Junta de Castilla y León (VA317P18, Infrared2018-UVA06), Interreg V España Portugal POCTEP (0624_2IQBIONEURO_6_E) and Centro en Red de Medicina Regenerativa y Terapia Celular de Castilla y León. The authors thank. Olga Shebanova and Andy Smith from Diamond Light Source for helping to test the WAXS.

Conflict of Interest

The authors declare no conflict of interest.

Data Availability Statement

The data that support the findings of this study are available in the supplementary material of this article.

Keywords

disinfector-assisted reduction, melanoma, photothermal treatment, reduced graphene oxide-protein, surgical dressing

Received: May 21, 2022
Revised: June 7, 2022
Published online:

[1] C. G. Watts, M. Dieng, R. L. Morton, G. J. Mann, S. W. Menzies, A. E. Cust, *Br J Dermatol* **2015**, *172*, 33.
[2] L. E. Davis, S. C. Shalin, A. J. Tackett, *Cancer Biol. Ther.* **2019**, *20*, 1366.
[3] P. G. L. Koolen, T. R. Matos, A. M. S. Ibrahim, J. Sun, B. T. Lee, R. A. Frankenthaler, S. J. Lin, *Plast. Reconstr. Surg. – Glob. Open* **2017**, *5*.
[4] G. C. Leonardi, L. Falzone, R. Salemi, A. Zanghì, D. A. Spandidos, J. A. Mccubrey, S. Candido, M. Libra, *Int. J. Oncol.* **2018**, *52*, 1071.
[5] B. Domingues, J. Lopes, P. Soares, H. Populo, *ImmunoTargets Ther.* **2018**, *7*, 35.
[6] M. C. Foletto, S. E. Haas, *An. Bras. Dermatol.* **2014**, *89*, 301.
[7] Z. Sobhani, M. A. Behnam, F. Emami, A. Dehghanian, I. Jamhiri, *Int. J. Nanomed.* **2017**, *12*, 4509.
[8] H. S. Jung, W. H. Kong, D. K. Sung, M.-Y. Lee, S. E. Beack, D. H. Keum, K. S. Kim, S. H. Yun, S. K. Hahn, *ACS Nano* **2014**, *8*, 260.
[9] Z. Li, H. Huang, S. Tang, Y. Li, X. F. Yu, H. Wang, P. Li, Z. Sun, H. Zhang, C. Liu, P. K. Chu, *Biomaterials* **2016**, *74*, 144.
[10] Y. Shi, M. Liu, F. Deng, G. Zeng, Q. Wan, X. Zhang, Y. Wei, *J. Mater. Chem. B* **2017**, *5*, 194.
[11] L. Ou, B. Song, H. Liang, J. Liu, X. Feng, B. Deng, T. Sun, L. Shao, *Part. Fibre Toxicol.* **2016**, *13*, 57.
[12] Z. Yang, Z. Sun, Y. Ren, X. Chen, W. Zhang, X. Zhu, Z. Mao, J. Shen, S. Nie, *Mol. Med. Rep.* **2019**, *20*, 5.
[13] B. Liu, S. Salgado, V. Maheshwari, J. Liu, *Curr. Opin. Colloid Interface Sci.* **2016**, *26*, 41.
[14] X. Xu, X. Mao, Y. Wang, D. Li, Z. Du, W. Wu, L. Jiang, J. Yang, J. Li, *Int. J. Biol. Macromol.* **2018**, *116*, 492.
[15] D. Konios, M. M. Stylianakis, E. Stratakis, E. Kymakis, *J. Colloid Interface Sci.* **2014**, *430*, 108.
[16] D. Li, T. Liu, X. Yu, D. Wu, Z. Su, *Polym. Chem.* **2017**, *8*, 4309.
[17] J. Wang, H. Wang, Y. Wang, J. Li, Z. Su, G. Wei, *J. Mater. Chem. B* **2014**, *2*, 7360.
[18] Y. Wu, G. M. Fortunato, B. O. Okesola, F. L. P. Di Brocchetti, R. Suntornnond, J. Connelly, C. De Maria, J. C. Rodriguez-Cabello, G. Vozzi, W. Wang, A. Mata, *Biofabrication* **2021**, *13*, 035027.
[19] D.-W. Park, A. A. Schendel, S. Mikael, S. K. Brodnick, T. J. Richner, J. P. Ness, M. R. Hayat, F. Atry, S. T. Frye, R. Pashaie, S. Thongpang, Z. Ma, J. C. Williams, *Nat. Commun.* **2014**, *5*, 1.
[20] M.-C. Wu, A. R. Deokar, J.-H. Liao, P.-Y. Shih, Y.-C. Ling, *ACS Nano* **2013**, *7*, 1281.

[21] J. T. Robinson, S. M. Tabakman, Y. Liang, H. Wang, H. S. Casalongue, D. Vinh, H. Dai, *J. Am. Chem. Soc.* **2011**, *133*, 6825.
[22] X. Guo, N. Mei, *J. Food Drug Anal.* **2014**, *22*, 105.
[23] J. Yin, Z. Dong, Y. Liu, H. Wang, A. Li, Z. Zhuo, W. Feng, W. Fan, *Carbon* **2020**, *169*, 182.
[24] D. Zhang, Z. Zhang, Y. Liu, M. Chu, C. Yang, W. Li, Y. Shao, Y. Yue, R. Xu, *Biomaterials* **2015**, *68*, 100.
[25] B. Chen, L. Jiang, J. Wu, A. Hu, X. Lu, Q. Jiang, *ChemNanoMat* **2019**, *5*, 1317.
[26] S. Stankovich, D. A. Dikin, G. H. B. Dommett, K. M. Kohlhaas, E. J. Zimney, E. A. Stach, R. D. Piner, S. B. T. Nguyen, R. S. Ruoff, *Nature* **2006**, *442*, 282.
[27] J. Gao, F. Liu, Y. Liu, N. Ma, Z. Wang, X. Zhang, *Chem. Mater.* **2010**, *22*, 2213.
[28] Y. Wu, B. O. Okesola, J. Xu, I. Korotkin, A. Berardo, I. Corridori, F. Luigi, J. Kanczler, J. Feng, W. Li, Y. Shi, V. Farafonov, Y. Wang, R. F. Thompson, M. M. Titirici, D. Nerukh, S. Karabasov, R. O. C. C. Oreffo, J. C. Rodriguez-cabello, G. Vozzi, H. S. Azevedo, N. M. Pugno, W. Wang, A. Mata, F. L. P. di Brocchetti, J. Kanczler, J. Feng, W. Li, Y. Shi, V. Farafonov, et al, *Nat. Commun.* **2020**, *11*, 1182.
[29] Q. Wen, S. M. Mithieux, A. S. Weiss, *Trends Biotechnol.* **2020**, *38*, 280.
[30] D. R. Dreyer, S. Murali, Y. Zhu, R. S. Ruoff, C. W. Bielawski, *J. Mater. Chem.* **2011**, *21*, 3443.
[31] M. U. Graziano, K. U. Graziano, F. M. G. Pinto, C. Q. de Moraes Bruna, R. Q. de Souza, C. A. Lascala, *Rev. Lat.-Am. Enfermagem* **2013**, *21*, 618.
[32] M. M. Ribeiro, V. A. Neumann, M. C. Padoveze, K. U. Graziano, *Rev. Lat.-Am. Enfermagem* **2015**, *23*, 741.
[33] S. R. , H. CM, K. DE, K. SL, *Future Microbiol.* **2014**, *9*, 1123.
[34] G. Kampf, *J. Hosp. Infect.* **2018**, *98*, 331.
[35] S. Mukherjee, P. Sriram, A. K. Barui, S. K. Nethi, V. Veeriah, S. Chatterjee, K. I. Suresh, C. R. Patra, *Adv. Healthcare Mater.* **2015**, *4*, 1722.
[36] S. You, J. Yu, B. Sundqvist, L. A. Belyaeva, N. V. Avramenko, M. V. Korobov, A. V. Talyzin, *J. Phys. Chem. C* **2013**, *117*, 1963.
[37] Y. Qiu, F. Guo, R. Hurt, I. Külaots, *Carbon* **2014**, *72*, 215.
[38] M. Cai, D. Thorpe, D. H. Adamson, H. C. Schniepp, *J. Mater. Chem.* **2012**, *22*, 24992.
[39] A. Berardo, M. F. Pantano, N. M. Pugno, *Interface Focus* **2016**, *6*, 20150060.
[40] F. K. Storm, W. H. Harrison, R. S. Elliott, D. L. Morton, *Cancer Res.* **1979**, *39*, 2245.
[41] H. Ma, Q. Zhou, J. Chang, C. Wu, *ACS Nano* **2019**, *13*, 4302.
[42] C. Feng, J. Ouyang, Z. Tang, N. Kong, Y. Liu, L. Y. Fu, X. Ji, T. Xie, O. C. Farokhzad, W. Tao, *Matter* **2020**, *3*, 127.
[43] S. Cai, C. Wu, W. Yang, W. Liang, H. Yu, L. Liu, *Nanotechnol. Rev.* **2020**, *9*, 971.
[44] O. F. Kuzu, F. D. Nguyen, M. A. Noory, A. Sharma, *Cancer Metastasis Rev.* **2015**, *8s1*, CGM.S21214.
[45] K. W. Feldman, R. T. Schaller, J. A. Feldman, M. McMillon, *Pediatrics* **1978**, *62*, 1.
[46] K. Lategan, H. Alghadi, M. Bayati, M. F. de Cortalezzi, E. Pool, *Nanomaterials* **2018**, *8*, 125.